Finite Element Simulations of Dynamic Shear Rupture Experiments and Dynamic Path Selection along Kinked and Branched Faults

JOURNAL OF GEOPHYSICAL RESEARCH, VOL. 114, B08304, doi:10.1029/2008JB006174, 2009

Finite element simulations of dynamic shear rupture experiments and dynamic path selection along kinked and branched faults

Elizabeth L. Templeton,[1] Aurélie Baudet,[2] Harsha S. Bhat,[3,4] Renata Dmowska,[1,5] James R. Rice,[1,5] Ares J. Rosakis,[4] and Carl-Ernst Rousseau[6]

Received 27 October 2008; revised 4 March 2009; accepted 13 May 2009; published 13 August 2009.

[1] We analyze the nucleation and propagation of shear cracks along nonplanar, kinked, and branched fault paths corresponding to the configurations used in recent laboratory fracture studies by Rousseau and Rosakis (2003, 2009). The aim is to reproduce numerically those shear rupture experiments and from that provide an insight into processes which are active when a crack, initially propagating in mode II along a straight path, interacts with a bend in the fault or a branching junction. The experiments involved impact loading of thin Homalite-100 (a photoelastic polymer) plates, which had been cut along bent or branched paths and weakly glued back together everywhere except along a starter notch near the impact site. Strain gage recordings and high-speed photography of isochromatic lines provided characterization of the transient deformation fields associated with the impact and fracture propagation. We found that dynamic explicit 2-D plane-stress finite element analyses with a simple linear slip-weakening description of cohesive and frictional strength of the bonded interfaces can reproduce the qualitative rupture behavior past the bend and branch junctions in most cases and reproduce the principal features revealed by the photographs of dynamic isochromatic line patterns. The presence of a kink or branch can cause an abrupt change in rupture propagation velocity. Additionally, the finite element results allow comparison between total slip accumulated along the main and inclined fault segments. We found that slip along inclined faults can be substantially less than slip along the main fault, and the amount depends on the branch angle and kink or branch configuration.

Citation: Templeton, E. L., A. Baudet, H. S. Bhat, R. Dmowska, J. R. Rice, A. J. Rosakis, and C.-E. Rousseau (2009), Finite element simulations of dynamic shear rupture experiments and dynamic path selection along kinked and branched faults, *J. Geophys. Res.*, *114*, B08304, doi:10.1029/2008JB006174.

1. Introduction

[2] Mature faults that play host to large earthquakes typically exhibit geometric complexities such as step overs, fault bends, and branches. These geometric complexities can play a major role in controlling earthquake rupture propagation and in many cases confine rupture extent. *Segall and Pollard* [1980] and *Sibson* [1986] found that steps in fault traces can impede or arrest earthquake rupture propagation. That work was extended by *Wesnousky* [1988, 2006], who added many more observations of stopping of large earthquakes caused by step overs, and discussed the implications of those observations on predicting the endpoints of future earthquakes. Other geologic studies have investigated the role of fault bends and changes in strike and found that those also correlated with sites of rupture termination and nucleation [*King and Nabelek*, 1985].

[3] Multiple numerical investigations have been conducted to determine how step overs, bends, and branches control rupture dynamics and propagation extent and to explain geological observations of the role of such complexities. *Harris et al.* [1991] and *Harris and Day* [1993, 1999], in a series of works, first investigated numerically the effect of fault steps on dynamic rupture using a finite difference method to determine the maximum compressional and dilational fault steps that can be taken during dynamic rupture propagation. Other studies including those by *Aochi et al.* [2000a, 2000b], *Duan and Oglesby* [2005], *Ando et al.* [2007], and *Adda-Bedia and Madariaga* [2008] have focused on the role of a change in fault strike during a single and repeated earthquake rupture. The criteria for branching

[1]School of Engineering and Applied Sciences, Harvard University, Cambridge, Massachusetts, USA.
[2]Chatou, France.
[3]Department of Earth Sciences, University of Southern California, Los Angeles, California, USA.
[4]Graduate Aerospace Laboratories, California Institute of Technology, Pasadena, California, USA.
[5]Department of Earth and Planetary Sciences, Harvard University, Cambridge, Massachusetts, USA.
[6]Department of Mechanical Engineering, University of Rhode Island, Kingston, Rhode Island, USA.

0148-0227/09/2008JB006174$09.00

during dynamic rupture in natural fault systems have been proposed from theoretical considerations and extensively studied numerically [*Poliakov et al.*, 2002; *Kame et al.*, 2003; *Bhat et al.*, 2004, 2007b; *Duan and Oglesby*, 2007]. In particular, *Poliakov et al.* [2002] investigated the dynamic stress field surrounding a rapidly propagating semi-infinite nonsingular mode II slip-weakening shear rupture in an elastic material to identify locations of possible branch activation, and found that the location of zones where the near-crack-tip stress field could violate a Mohr-Coulomb failure criterion, and potentially nucleate rupture along a preexisting branch, depends on the preexisting stress state as well as the rupture velocity at the junction. *Kame et al.* [2003], *Bhat et al.* [2004] and *Fliss et al.* [2005] extended the study of *Poliakov et al.* [2002] to investigate how rupture velocity and branch angle affect branching with a focus on explaining branch activation during recent large earthquakes such as the 1992 Landers earthquake [*Fliss et al.*, 2005], the 2002 Denali earthquake [*Bhat et al.*, 2004], and other cases [*Kame et al.*, 2003]. Those numerical studies can be used to make predictions about dynamic path selection of rupture propagation for frictional slip-weakening rupture.

[4] Experiments have also been conducted to investigate the role of complexities during earthquakes in a laboratory setting (for a thorough review, see *Rosakis et al.* [2007]). The experimental studies by *Rousseau and Rosakis* [2003, 2009] investigated the role of a change in fault strike and the effect of a branch junction during mode II rupture propagation along confined paths in Homalite plates. The effects of short branches extending from a main fault during dynamic rupture was studied by *Biegel et al.* [2007] during laboratory earthquakes along a fault in Homalite plates. They found that depending on the branch angle and length, those small branches could have a large effect on rupture velocity along the main fault (see also the theoretical work by *Bhat et al.* [2007b]).

[5] The aim of this paper is to reproduce numerically the shear rupture experiments in Homalite plates and from that provide an insight into dynamic rupture path selection. We conduct finite element analyses to model crack propagation in thin plates with fault geometries in the same configurations as in the experiments by *Rousseau and Rosakis* [2003, 2009]. The aim is to understand what happens when a crack, initially propagating in mode II along a straight path, reaches a bend in the fault path or a branching junction. We show that a simple slip-weakening description of fault strength can be used to reproduce the experimental results. We attempt to quantify the relationship between inclined fault angle and post junction rupture velocity, and, for a branched fault system, we examine the relationship between dynamic path selection and branch incline angle.

2. Theoretical Background

[6] The near-crack-tip stress field surrounding a shear crack plays a large role in governing rupture behavior. Figure 1 shows the coordinate system and stress state ahead of a mode II shear rupture, where the rupture is in the η_1 direction and is right-lateral, like those studied numerically in this paper. The stress which would have been transmitted if there was no cracking has the form

$$\sigma_{ij}^{nc} = \begin{bmatrix} \sigma_{xx}^{nc} & \sigma_{xy}^{nc} & 0 \\ \sigma_{xy}^{nc} & \sigma_{yy}^{nc} & 0 \\ 0 & 0 & \sigma_{zz}^{nc} \end{bmatrix} \tag{1}$$

In previous numerical works investigating the effects of geometric complexities during dynamic shear crack propagation such as those of *Poliakov et al.* [2002], *Kame et al.* [2003], and *Bhat et al.* [2007b], the far-field regional static stress state is taken as the no-crack stress state. In those works, the angle, Ψ, that the initial most compressive stress prior to rupture makes with the fault largely determines the location of damage and microcracking as well as branch activation. In the experiments of *Rousseau and Rosakis* [2003, 2009] that are analyzed here, mode II shear rupture is initiated by impact of a steel projectile traveling at a velocity v_i with the Homalite specimen, and the stress transmitted if there is no cracking is the time-dependent field generated by that impact. Homalite is a photoelastic material, and high-speed digital photographs taken during the experiment display the dynamic stress field, crack propagation and dynamic path selection during the rupture. In Figure 2 photographs of isochromatic fringe patterns, lines of constant difference between the in-plane principal stresses, show the dynamic no-crack stress field produced by the impact alone, where the impact is modeled using a velocity boundary condition, to be discussed in section 3, for an impact speed of 7 m/s.

[7] The total stress field during rupture can be written as a combination of the stress which would have been transmitted if there was no cracking, which is time dependent for this study, and the stress alteration due to the cracking. It is given by

$$\sigma_{ij} = \sigma_{ij}^{nc} + \Delta\sigma_{ij} \tag{2}$$

where $\Delta\sigma_{ij}$ is the alteration due to the cracking process. Figure 1 shows the stress state ahead of the rupture tip. The impact loading generates a compressive stress, σ_{xx}, in the upper half of the specimen where the loading is applied. The magnitude of that stress is, nominally,

$$\sigma_{xx} = \frac{E}{1-\nu^2}\frac{v_i}{\hat{c}_p} \tag{3}$$

where E and ν are the Young's modulus and Poisson ratio, and $\hat{c}_p$ is the 2-D plane-stress P wave speed,

$$\hat{c}_p = \sqrt{\frac{E}{\rho(1-\nu^2)}} \tag{4}$$

Near the crack tip, $\Delta\sigma_{ij}$ can increase significantly over the surrounding prestress, but the works of *Kame et al.* [2003] and *Bhat et al.* [2004] showed that prestress field at the crack tip plays a large role in determining path selection for rupture continuation along a nonplanar or branched fault geometry.

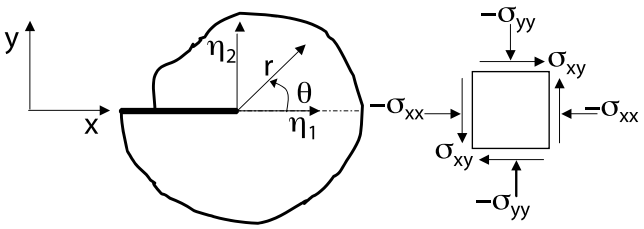

Figure 1. Schematic showing coordinate system convention and stress state ahead of the rupture.

2.1. Supershear Crack-Tip Stress Field

[8] Mode II shear ruptures can propagate in two speed regimes, at speeds below the Rayleigh wave speed and speeds between the shear wave speed and the P wave speed [*Andrews*, 1976; *Burridge et al.*, 1979]. Field observations indicate that the majority of earthquake ruptures propagate in the sub-Rayleigh regime, but there are several cases with evidence of rupture apparently propagating in the supershear regime, such as the 1979 Imperial Valley [*Archuleta*, 1984; *Spudich and Cranswick*, 1984], 1999 Izmit [*Bouchon et al.*, 2000, 2001], 2001 Kunlun [*Bouchon and Vallée*, 2003; *Robinson et al.*, 2006; *Vallée et al.*, 2008], and 2002 Denali [*Ellsworth et al.*, 2004; *Dunham and Archuleta*, 2004; *Aagaard and Heaton*, 2004; *Bouchon and Karabulut*, 2008] earthquakes. Laboratory experiments involving mode II rupture along preweakened paths in Homalite plates have displayed definitive evidence of supershear rupture with clearly visible Mach fronts [*Rosakis et al.*, 1999; *Rousseau and Rosakis*, 2003, 2009; *Xia et al.*, 2004, 2005; *Biegel et al.*, 2007; *Rosakis et al.*, 2007].

[9] In this study, we focus on modeling the experiments of *Rousseau and Rosakis* [2003, 2009] which involve cracks propagating at a supershear speed. To gain some understanding of which inclined fault paths are dynamically favorable for continued crack propagation, we next present the analytical expressions for stresses near a crack tip propagating at a supershear speed. Consider a mode II crack propagating in an unbounded, elastic homogeneous medium that is confined to its own plane so that it cannot kink or curve from its prescribed, straight path. Let there be a Cartesian coordinate system (η_1, η_2) moving with the crack tip with related polar coordinates (r, θ) as shown in Figure 1. The origin, (x, y), is related to the moving cartesian coordinate system, (η_1, η_2), by

$$\eta_1 = x - \int_0^t v(t')dt', \quad \eta_2 = y \tag{5}$$

The asymptotic form of the stress and deformation field for a crack propagating dynamically in the supershear regime was determined by *Freund* [1990] and repeated by *Rousseau and Rosakis* [2003] as:

$$\sigma_{xx} = \frac{K_{II}^{*d}}{2\alpha_p\sqrt{2\pi}}\left[\frac{-\left(1+2\alpha_p^2+\hat{\alpha}_s^2\right)}{r_p^q}\sin\left(q\theta_p\right) + \frac{\left(1-\hat{\alpha}_s^2\right)\sin[\mathrm{sgn}(\eta_2)q\pi]}{(-\eta_1-\hat{\alpha}_s|\eta_2|)^q}H(\eta_1-\hat{\alpha}_s|\eta_2|)\right] \tag{6}$$

$$\sigma_{yy} = \frac{K_{II}^{*d}}{2\alpha_p\sqrt{2\pi}}\left[\frac{\left(1-\hat{\alpha}_s^2\right)}{r_p^q}\sin\left(q\theta_p\right) - \frac{\left(1-\hat{\alpha}_s^2\right)\sin[\mathrm{sgn}(\eta_2)q\pi]}{(-\eta_1-\hat{\alpha}_s|\eta_2|)^q}H(\eta_1-\hat{\alpha}_s|\eta_2|)\right] \tag{7}$$

$$\sigma_{xy} = \frac{K_{II}^{*d}}{2\sqrt{2\pi}}\left[\frac{1}{r_p^q}\cos\left(q\theta_p\right) - \frac{\cos[\mathrm{sgn}(\eta_2)q\pi]}{(-\eta_1-\hat{\alpha}_s|\eta_2|)^q}H(\eta_1-\hat{\alpha}_s|\eta_2|)\right] \tag{8}$$

Where K^{*d}_{II} is the dynamic stress intensity factor for supershear crack growth, α_p and $\hat{\alpha}_s$ are defined as:

$$\alpha_p = \sqrt{1-\left(v/\hat{c}_p\right)^2} \quad \hat{\alpha}_s = \sqrt{(v/c_s)^2-1} \tag{9}$$

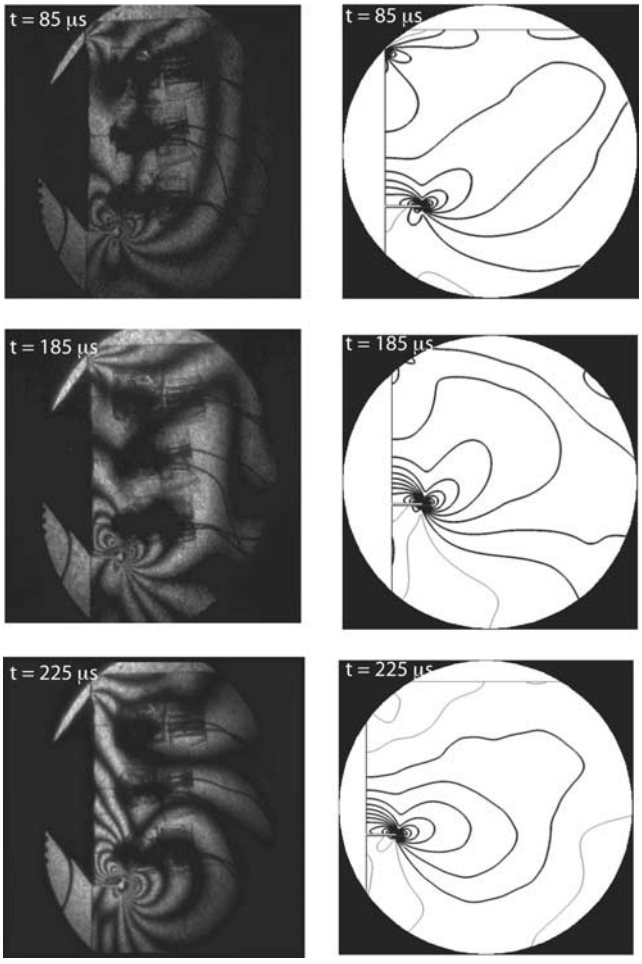

Figure 2. Comparison of isochromatic fringe patterns, contours of lines of constant difference between in-plane principal stresses, for several times after impact between (left) experiments and (right) numerical simulations for a Homalite-100 plate with a notch impacted by a projectile traveling at 7 m/s. Three strain gages were placed on the plates during the experiment to measure the dynamic strains and can be seen in the photographs.

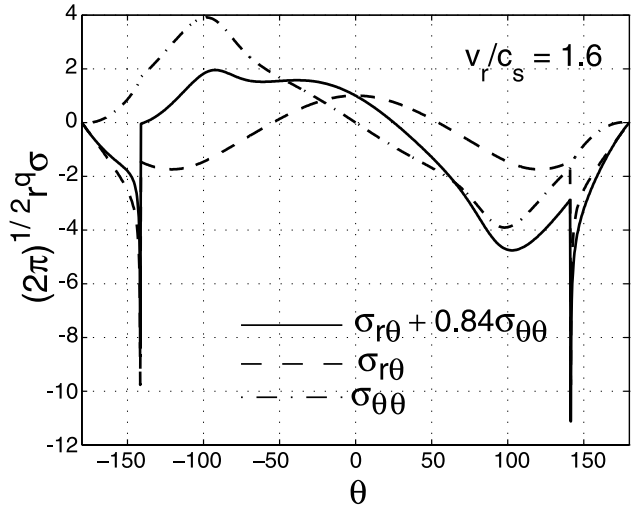

Figure 3. Angular variation in stress ahead of the crack tip normalized by r_p^q/K_{II}^{*d}.

The scaled polar coordinates, (r_p, θ_p) are defined by:

$$r_p = \sqrt{\eta_1^2 + \alpha_p^2 \eta_2^2} \quad \theta_p = \arctan \frac{\alpha_p \eta_2}{\eta_1} \tag{10}$$

The strength of the crack tip singularity, q, depends on the crack speed, v. When $v = c_s$, the shear wave speed, $q = 0$; q increases monotonically to $q = 1/2$ when $v = \sqrt{2}c_s$ then decreases monotonically to 0 when $v = \hat{c}_p$. The exponent, q, is given by:

$$q = \frac{1}{\pi} \arctan \left[\frac{4\alpha_p \hat{\alpha}_s}{\left(1 - \hat{\alpha}_s^2\right)^2} \right] \tag{11}$$

[10] Equations (6)–(8) are valid when the singular terms at the crack tip are more significant than the remainder of the expression. The singular stresses govern deformation in the immediate vicinity of the crack tip while overall geometry and loading configuration govern behavior farther from the crack tip. The supershear solution has a discontinuity in stresses due to the Heaviside function which translates into the formation of two edges of the Mach cone. The singularity in the stresses exists not only at the crack tip, but along the Mach front as well. At the special speed of $v = \sqrt{2}c_s$, the Mach front disappears, and the singularity exists only at the crack tip.

2.2. Angular Stress Distribution Around the Dynamic Shear Crack

[11] The angular variation of the stress field, as given by equations (6)–(8), provides a rough determination of which branch or bend angles are dynamically favorable for rupture propagation. The stresses can be expressed in terms of σ_{rr}, $\sigma_{r\theta}$ and $\sigma_{\theta\theta}$, the radial, shear and hoop stresses. Since the crack is advancing because of shear loading, and radial stresses act in the direction of crack growth, $\sigma_{r\theta}$ and $\sigma_{\theta\theta}$ are the relevant stresses to examine at the crack tip, and $\sigma_{r\theta}$ will be the dominating stress component. In Figure 3, the shear and hoop stresses, and a combination of them, are plotted for a rupture velocity of $v = 1.6c_s$, a typical velocity reached immediately before the fault bend or branching junction in both the experiments and the numerical simulations that follow, as a function of angular location and normalized by r_p^q/K^{*d}_{II}. There are three extrema in the shear stress at $\theta = 0°$ and at $\theta = \pm 141°$, and the shear stress is symmetric about $\theta = 0$. Since the shear stress is symmetric, branching to either side of the fault would be equally likely for a failure criterion that does not depend on $\sigma_{\theta\theta}$. The hoop stress, $\sigma_{\theta\theta}$, is positive for negative branch angles, while it is negative for positive angles, so the hoop stress favors crack growth for branches inclined at negative angles from the main fault. There is an infinite stress jump in the shear stress at $\pm 141°$ which corresponds to the location of the Mach cone. As crack speed increases, the location of the discontinuity shifts

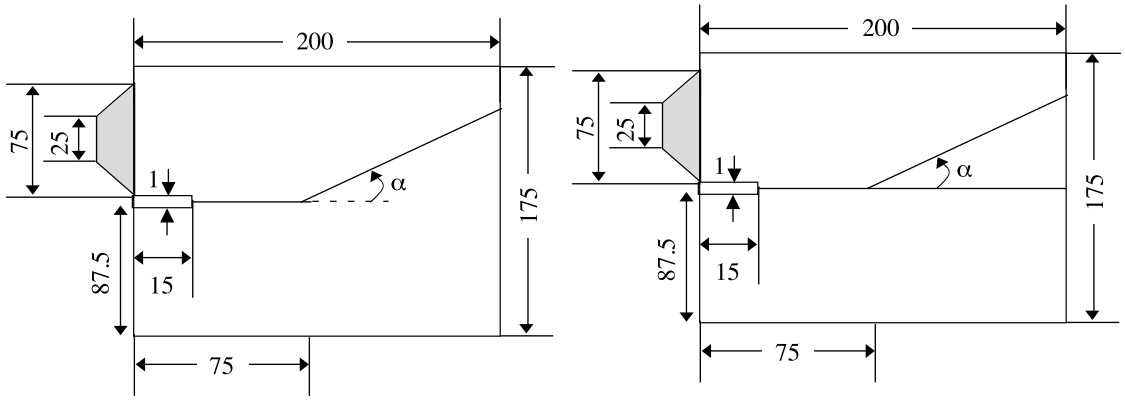

Figure 4. Geometry of the 5 mm thick Homalite-100 plate with steel buffer used in (left) kinked and (right) branched fault experiments. All dimensions are in mm. Positive and negative kink and branch fault inclination angles, α, were considered. For positive α, the secondary fault is on the compressional side of rupture along the main fault, that is, the side experiencing compressional fault parallel strain ahead of the rupture. The secondary fault is on the extensional side for negative α.

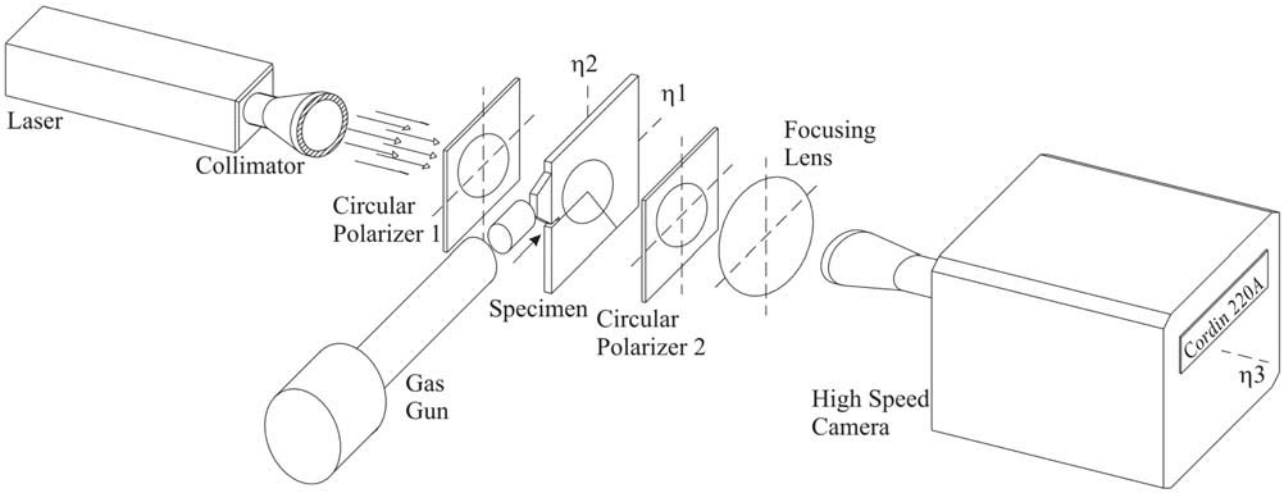

Figure 5. Schematic of the experimental dynamic photoelastic setup and high-speed camera from the experiments of *Rousseau and Rosakis* [2003, 2009].

toward larger angles with its position given by $\theta = (\pi - \sin^{-1}[c_s/v])$.

3. Experimental and Numerical Models

[12] In the experiments, two predefined fault configurations were used: a fault with a bend [*Rousseau and Rosakis*, 2003] and a branched fault geometry [*Rousseau and Rosakis*, 2009] as shown in Figure 4. In this paper we analyze numerically, using the finite element method, shear dominated cracks propagating along branched and kink paths in the configurations like those studied experimentally. In this section, we first review the experimental methodology used by *Rousseau and Rosakis* [2003, 2009] and then detail the simulation techniques and parameter choices used to numerically simulate the experiments.

3.1. Experimental Procedure

[13] The experiments were done with plates of Homalite-100, a birefringent polymer, which has a Young's modulus $E = 5.2$ GPa, a Poisson ratio $\nu = 0.34$, and a density $\rho = 1230$ kg/m^3 at strain rates in excess of 10^3 s^{-1} (as listed by *Rousseau and Rosakis* [2009]). The plane-stress longitudinal, shear, and Rayleigh wave speeds are $\hat{c}_p = 2186$ m/s, $c_s = 1243$ m/s, $c_R = 1005$ m/s. The plates were 5 mm thick, 175 mm high, and 200 mm long, and as shown in Figure 4 had preweakened paths setting the fault geometry. This plate geometry ensured the prevalence of two-dimensional, generalized plane-stress conditions, although the 3-D constraint induced a state approaching 2-D plane strain very close to the crack tip [*Rosakis and Ravi-Chandar*, 1986]. The preweakened paths were created by cutting the specimens into two parts for kinked paths or three parts for branched paths, and bonding those parts using a polyester resin with weakened fracture properties with respect to the bulk material, but similar elastic properties and density, as measured by *Samudrala et al.* [2002]. Figure 5 shows a schematic of the experimental setup. A starter notch machined along the horizontal interface, 1 mm wide and 15 mm long, ensured nearly pure mode II initiation of the loading and prevented the immediate transmission of impact stress waves applied to the top of the specimen to the bottom half of the specimen. A shear crack was initiated by impact of a hardened steel projectile with a steel buffer bonded to the top half of the specimen near the notch. *Rousseau and Rosakis* [2009] chose impact speeds of 20 m/s and 30 m/s to generate sub-Rayleigh and supershear ruptures, respectively. The shear crack, initiated at the notch tip, propagates along the interface in a right-lateral manner. The weak predefined paths force the crack to remain on the prescribed interface and retain its imposed mode II state. During each experiment, the dynamic stress field in the photoelastic Homalite specimen was captured using high-speed photography.

3.2. Numerical Model and Procedure

[14] We used the explicit dynamic finite element method, in the form of ABAQUS/Explicit [*ABAQUS, Inc.*, 2005] to simulate the experiments. A 2-D rectangular mesh with a notch, as shown in Figure 6, composed of 3-noded linear plane-stress elements (type CPS3 in ABAQUS) was used. The elements were arranged in a cross-triangle pattern, as illustrated in Figure 7. The impact was simulated using a time-dependent velocity boundary condition, as done by *Needleman and Rosakis* [1999]. Along the location of the buffer, a velocity boundary condition was instead imposed in the finite element model as shown in Figure 6. At time $t = 0$ the velocity is ramped linearly from $v = 0$ to v_i over a rise time $t_R = 20$ μs. The velocity is then held constant at v_i along the boundary at the buffer location for the remaining 80 μs of the analysis.

$$v(t) = \begin{cases} v_i t/t_R, & 0 < t < t_R \\ v_i, & t_R < t \end{cases} \tag{12}$$

The 20 μs rise time was used to account for the travel time of a longitudinal wave across the steel buffer. The velocity at the interface between the steel buffer and Homalite plate, is v_i, an impedance corrected velocity which differs from the projectile velocity by 1.6%. Use of the velocity boundary condition reduces computation time and eliminates the complexities associated with modeling the full impact

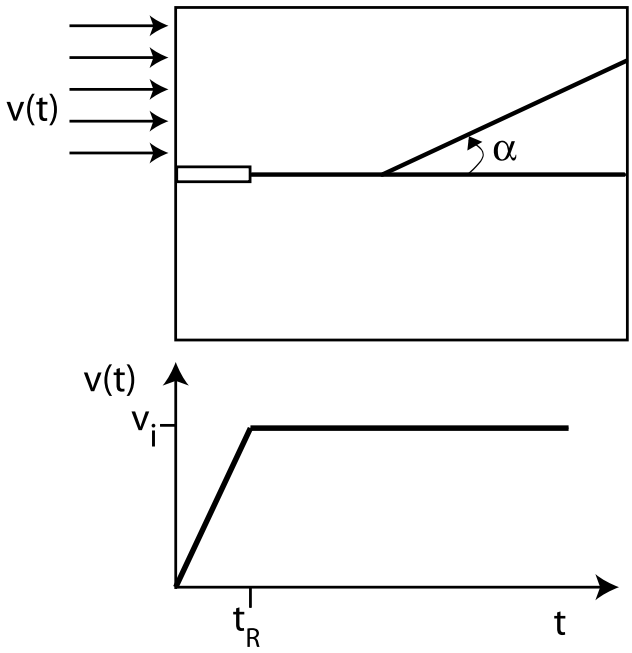

Figure 6. Finite element model geometry. Impact is modeled using a velocity boundary condition where the velocity increases from 0 to the impact velocity, v_i, over a rise time of 20 μs.

problem. Figure 2 compares numerically produced isochromatic fringe patterns to photographs of isochromatic fringe patterns generated by the loading alone with no crack propagation. Although there is not perfect agreement, the numerical analyses produce the three lobes observed around the notch tip. The performance of the velocity boundary condition was verified by comparison of model and experimental results for an experiment in which no cracking was allowed. Strains at three locations, as shown in Figure 8, were compared to strain gage data collected in an experiment of impact for a plate with a notch but no weakened path. The strains determined by the finite element model are a reasonable, although far from close, approximation to the strain gage data from the experiment, as seen in Figure 8. Comparison of photographs of the isochromatic fringe patterns taken during the experiment to contour lines of $\sigma_1-\sigma_2$ from the finite element analysis (Figure 2) shows

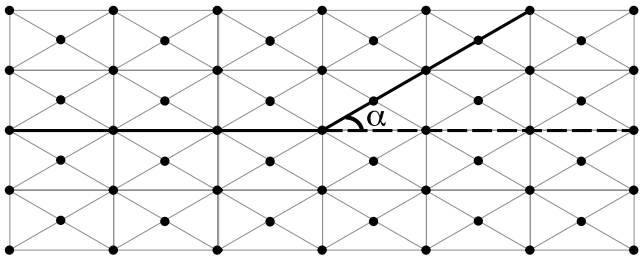

Figure 7. Finite element model geometry, shown here for a branch angle $\alpha = 30°$. Triangular plane-stress elements with three nodes are used. Elements are arranged in a cross triangle pattern.

that in both the experiment and the finite element analysis, the general shape of the isochromatic fringes are the same in that vicinity, if not at the impact site. Around the vicinity of the notch, there is a region of stress concentration. Nearly vertical contours in the top left of the specimen show strain caused by longitudinal waves propagating from the impact. On the basis of the comparison of the strain gage data and the isochromatic fringe patterns, the velocity boundary condition imposed provides an acceptable approximation to the full impact problem for our purposes here.

[15] The slip-weakening formulation proposed by *Ida* [1972] and *Palmer and Rice* [1973] is widely used as a simplified failure criterion to describe the earthquake rupture process and was used here as the failure criterion to describe the evolution of shear strength with slip along the bonded, predefined fault paths. The principal assumption in the slip-weakening law is that frictional strength, at fixed normal stress, depends only on the amount of slip, Δu, that has occurred on the fault. In the simplest case of linear degradation of frictional strength with slip, and assumptions of incohesive Coulomb friction, the frictional strength of the fault can be written as

$$\tau = f(\Delta u) \times (-\sigma_n) \tag{13}$$

where $f(\Delta u)$ describes the evolution of the coefficient of friction with increasing slip,

$$f(\Delta u) = \begin{cases} f_s - (f_s - f_d)\dfrac{\Delta u}{D_c}, & \Delta u < D_c \\ f_d, & \Delta u > D_c \end{cases} \tag{14}$$

Here, D_c is the critical slip-weakening distance. The peak and residual shear stress, $\tau_p = f_s \times (-\sigma_n)$ and $\tau_r = f_d \times (-\sigma_n)$

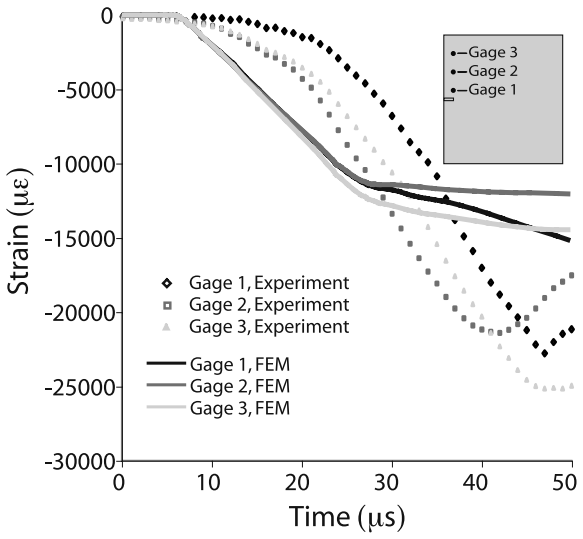

Figure 8. Comparison of strain gage data from experiments and finite element results for impact of a Homalite-100 plate with no preweakened fault path for a projectile velocity of 23.5 m/s. The simulation and experimental results match well initially, but differences develop in part because of 3-D effects.

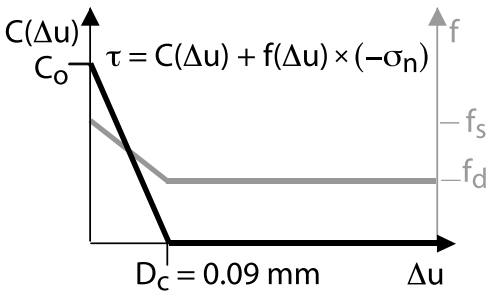

Figure 9. The strength of the preweakened faults bonded with a polyester resin in the experiments is described in the numerical model by a cohesive and frictional slip-weakening law.

$(-\sigma_n)$ are both proportional to a static or dynamic coefficient of friction times the fault-normal stress, $(-\sigma_n)$. The fault strength should also include a cohesive component due to the glue bonding the two surfaces. A slip-weakening law, with the same slip-weakening distance, D_c, was used to describe evolution of the cohesive component of fault strength for its initial level, C_o, to zero.

$$C(\Delta u) = \begin{cases} C_o\left(1 - \dfrac{\Delta u}{D_c}\right), & \Delta u < D_c \\ 0, & \Delta u > D_c \end{cases} \tag{15}$$

We combined the cohesive and fictional slip - weakening terms as follows, and illustrated in Figure 9, to describe the shear strength of the bonded faults,

$$\tau = C(\Delta u) + f(\Delta u) \times (-\sigma_n) \tag{16}$$

[16] To define the preweakened surface, we use a split-node contact procedure (ABAQUS user subroutine *VFRIC*) to prescribe the weakened shear strength of the fault resulting from slip during rupture along the fault. Details of the split-node contact procedure and its implementation in ABAQUS are given by *Templeton and Rice* [2008]. Along each fault segment, a duplicate set of nodes is defined to create two surfaces. In this finite element modeling, the crack can only propagate along the predefined surfaces, and no cracking is allowed elsewhere in the plate. This model cannot describe the formation of new microcracks [*Samudrala et al.*, 2002; *Rosakis*, 2002], which form along the fault segments during several of the experiments, particularly along the inclined segment. During slip, tangential forces are applied at each node along the fault, consistent with the shear strength of the fault as given by equation (16).

[17] Along the initial fault path, the impact loading creates little normal stress, and the cohesive term in the slip-weakening law dominates. The frictional normal stress dependent term of equation (16) becomes important on the inclined kink and branch faults due to changes in normal stress caused by the impact loading and rupture along the horizontal fault. In the numerical analyses, the faults have zero tensile strength, and opening can occur wherever normal stress becomes tensile along the fault. Where the normal stress becomes tensile, the surfaces can come out of contact and are allowed to freely move past one another at that location on the contact surface until the surfaces come back into contact. (This is a simplification built in to the ABAQUS contact friction procedure that is sensible for predominantly compressive fields as we have in most of our bend and branch junction analyses.)

3.2.1. Parameter Choices for Fault Strength

[18] The bonding and decohesion properties used in the slip-weakening law, f_s, f_d, C_o, and D_c, define the frictional behavior of the fault. In order to better understand the influence of these on the experimental system, an investigation quantified the relationship between the frictional and cohesive shear strength properties of the interface and impact velocity and the predicted speed of rupture propagation. We investigated the relationship between cohesive strength, in terms of the ratio of the initial cohesive strength of the interface to a characteristic impact stress level, C_o/B, and the resulting rupture propagation velocity, where B, the nominal impact stress, is defined by

$$B = \frac{E}{1-\nu^2}\frac{v_i}{\hat{c}_p} \tag{17}$$

Linear and dimensional analyses show that the stress field, neglecting fracture processes, would be proportional to B times a function of length scales divided by $\hat{c}_p t$ and ν. The effect of the frictional strength on rupture velocity is investigated in terms of f_s, the static coefficient of friction, while holding the dynamic coefficient of friction constant at $f_d = 0.0$. The fracture energy can be estimated using the mode II fracture toughness:

$$G = \frac{1-\nu}{2\mu}K_{II,c}^2 = \frac{1}{2}C_o D_c \tag{18}$$

The mode II fracture toughness of the bond, $K_{II,c}$, as measured using a Brazil tensile strength test, is approximately 1.4 MPa $m^{1/2}$. Using equation (18), $D_c = 90$ μm for $C_o = 7.5$ MPa. For this parameter investigation, the critical slip-weakening distance, D_c is specified as a constant, $D_c = 90$ μm. Values of C_o/B ranging from 0.2 to 0.6 (corresponding to impact velocities ranging from 10 m/s to 30 m/s for $C_o = 15$ MPa or cohesive strengths, C_o, ranging from 5 MPa to 15 MPa for an impact velocity of 10 m/s), and values of the static coefficient of friction ranging from 0.00 to 0.84 were tested.

[19] Figure 10 shows the results of the parameter study, for a branched fault with a branch angle of +35°. Before reaching the branching junction, the rupture velocity depends mostly on C_o/B since there is little or no normal stress on the fault resulting from the impact loading. Increasing C_o/B results in the rupture velocity decreasing along the fault, although there is a slight increase in rupture velocity with increasing static coefficient of friction along the main fault before the branching junction. Consistent with experiments, the rupture velocity along the continuation of the main fault after the branching junction remains at $1.6c_s$ and has little dependence on C_o/B or f_s. Along the inclined fault on the compressional side, the rupture velocity near the branching junction depends primarily on f_s and

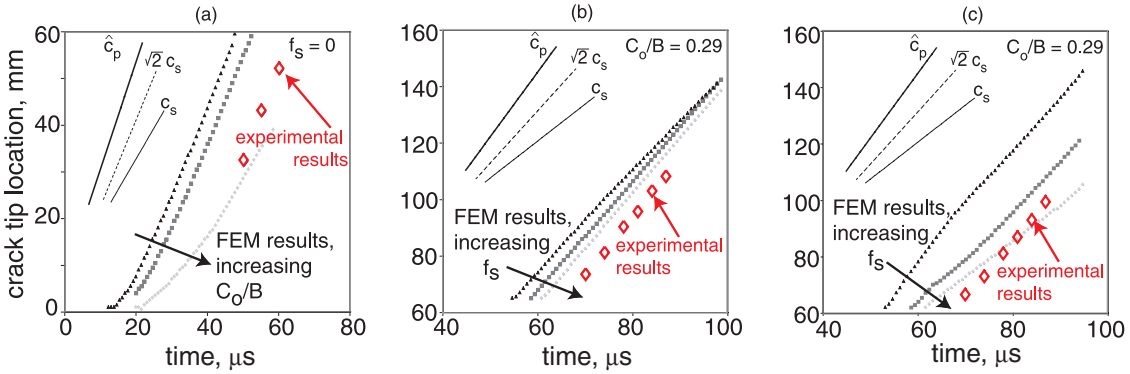

Figure 10. The dependence of rupture propagation on cohesive shear strength, C_o/B, and static friction coefficient, f_s along (a) the horizontal fault before the branch, (b) the horizontal fault after the branch, and (c) the inclined fault are shown. C_o/B = 0.20, 0.29, and 0.59 and f_s = 0.0, 0.50, and 0.84 for f_d = 0.

shows little dependence on C_o/B. As f_s increases, the rupture velocity on the inclined fault decreases.

[20] The cohesive strength and static coefficient of friction chosen for the numerical simulations match experimentally determined properties and produce the rupture velocities found experimentally. The static coefficient of friction is set to $f_s = 0.84$, the static friction coefficient of the bond as obtained by measuring the inclination angle at which sliding begins between two specimens. The peak cohesive strength, C_o, is set to 15 MPa, the shear strength of the fault in mode II based on Iosipescu shear test. To reproduce the supershear results, the projectile impact speed used is 30 m/s, the same speed used by *Rousseau and Rosakis* [2009] to generate supershear ruptures propagating toward the junction at a speed of $1.6c_s$.

4. Simulation Results

[21] The impact, as simulated with the velocity boundary condition described in section 3.2, causes a stress concentration to build at the notch tip which initiates a right-laterally propagating shear crack along the first fault segment. The crack accelerates to the supershear regime, propagating at a roughly constant speed of $1.6c_s$ prior to reaching the branching junction at the end of that first fault segment. Results for secondary kink or branch fault inclinations of ±10°, ±35°, and ±80° are presented next. For each inclination angle, two geometric configurations are presented: a fault bend with no continuation of the main fault, and a fault branch with main fault continuation after the branching junction. Bend or branch faults inclined at a negative angle to the main fault are on the extensional side of the rupture along the main fault, the side that experiences extensional fault parallel strains due to rupture. Secondary faults inclined at positive angle are on the compressional side.

[22] In the following sections, the behavior of the rupture after it reaches the branching junction is discussed. Simulation results showing the dynamic stress field are presented as isochromatic fringe patterns. Comparisons between the photographs of the isochromatic fringe patterns taken during the experiment and those produced in the numerical simulations along with comparisons of relative crack tip location during the experiments and numerical simulations are presented for each fault geometry. Figure 11 shows a comparison between the experimental and numerical isochromatic fringe patterns for the cases with inclined fault bends on the compressional side of the fault. Simulation times are selected to best match the rupture tip position in the photographs. In the experiments, a strain gage attached to the steel buffer triggers the camera to begin recording the event, so the absolute times in the simulations and experiments will be different because of this triggering. A Mach front can be seen after the first 30 μs, indicating that the rupture is propagating faster than the shear wave speed. After 50 μs, the crack tip reaches the branching junction, as can be seen in Figure 11.

4.1. Fault Kinks

[23] The first simulations model the experiments on faults with an abrupt kink encountered after the crack propagates along the main horizontal path for 60 mm. Four distinct rupture behaviors are observed numerically for those six cases: rupture continuation through the fault bend with no change in velocity, rupture continuation through the fault bend with a slow down in velocity at the bend, rupture termination after brief propagation along the bend, and rupture termination at the bend. Figures 11 and 12 show a comparison of the isochromatic fringe patterns observed in the experiments and those calculated in the finite element analyses for kinks to the compressional and extensional sides of the fault, respectively, at angles of 10°, 35°, and 80°. Figure 13 presents the evolution of crack tip position during the experiments and the numerical simulations for branches to both the compressional and extensional sides of the fault. The experimental data for crack tip position are shifted in time so that the time when the rupture reaches the branching junction is approximately the same for the experiments and the numerical simulations (timing of experimental results is affected by somewhat variable conditions in triggering of the camera).

[24] The kink angle controls how much, if at all, rupture velocity changes after the kink in the fault is encountered for the same impact velocity. For faults with a bend to the compressional or extensional side of the fault at a shallow angle of 10°, rupture propagates along the inclined fault at a supershear speed with no reduction of propagation velocity after the kink. For a kink angle of +35°, rupture propagates

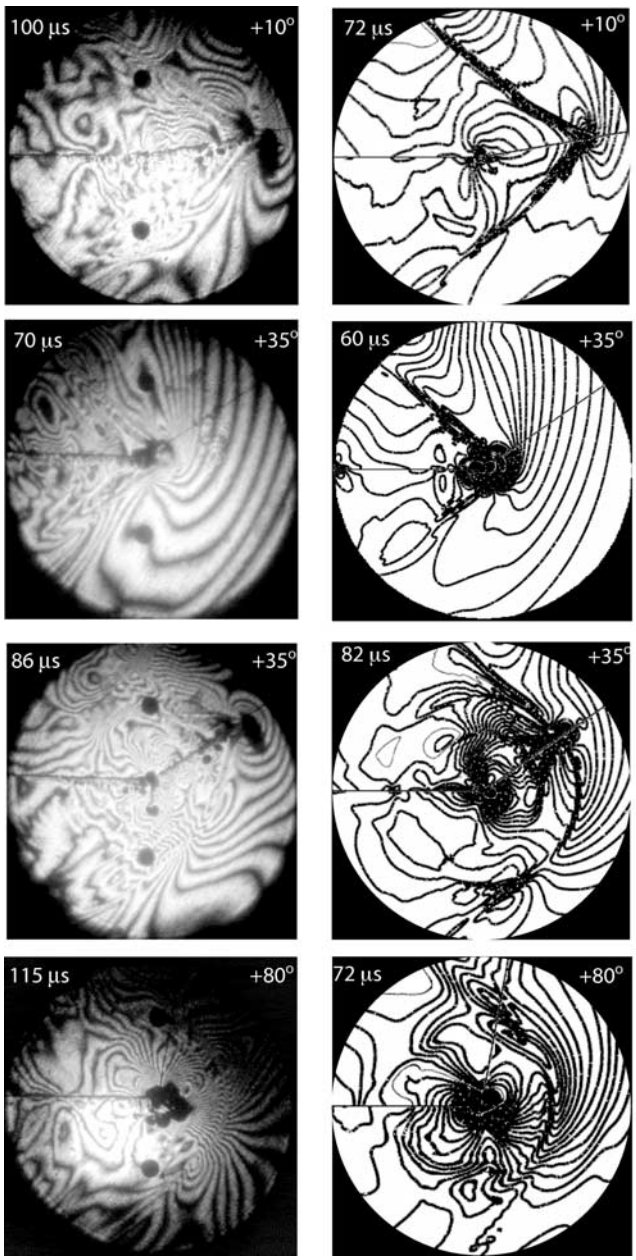

Figure 11. Comparison between (left) photographs of isochromatic fringe patterns and (right) finite element simulation results for kinked faults with the inclined branch on the compressional side.

along the inclined fault as well, but rupture velocity is initially sub-Rayleigh along the kinked fault, and the transition to supershear occurs after a short propagation distance. The cases with large angle fault bends show that those angles are less favorable for continued rupture propagation. When the kink angle is 80° to the extensional side, the rupture velocity along the inclined fault begins at a speed well above the P wave speed, but quickly slows down and stops propagating along the path after the crack has traveled 50 mm along the incline. Rupture ignores the inclined fault altogether for a kink angle of 80° to the compressional side, with no evidence of rupture propagation along the secondary inclined fault. The numerical observations agree with the experimental results for all kink angles studied. In addition to good agreement of the isochromatic fringe patterns, overall, the numerical results for crack tip position, as shown in Figure 13, match the experimental data well. The numerical results deviate from the experimental results for the 35° compressional kink, showing a prominent decrease in rupture velocity just past the fault kink. However, both the numerical and experimental isochromatic fringe patterns do suggest a slower rupture propagation along the kinked fault, as evidenced by lack of a clear Mach front (Figure 11), during the initial rupture propagation along the inclined fault.

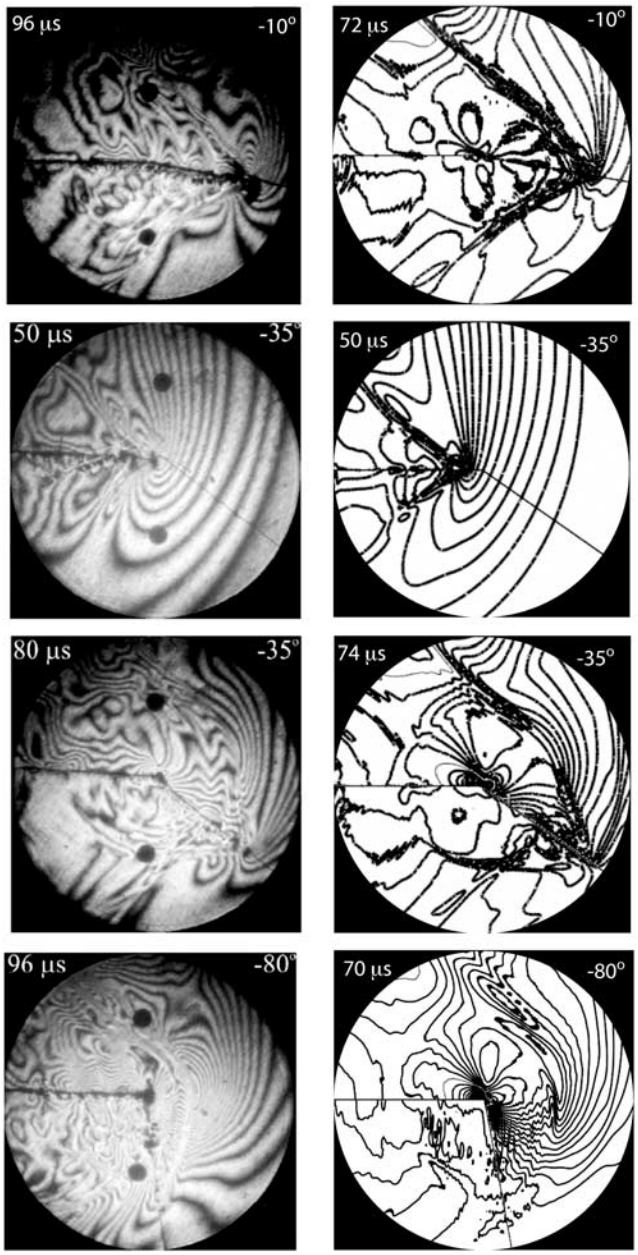

Figure 12. Comparison between (left) photographs of isochromatic fringe patterns and (right) finite element simulation results for kinked faults with the inclined branch on the extensional side.

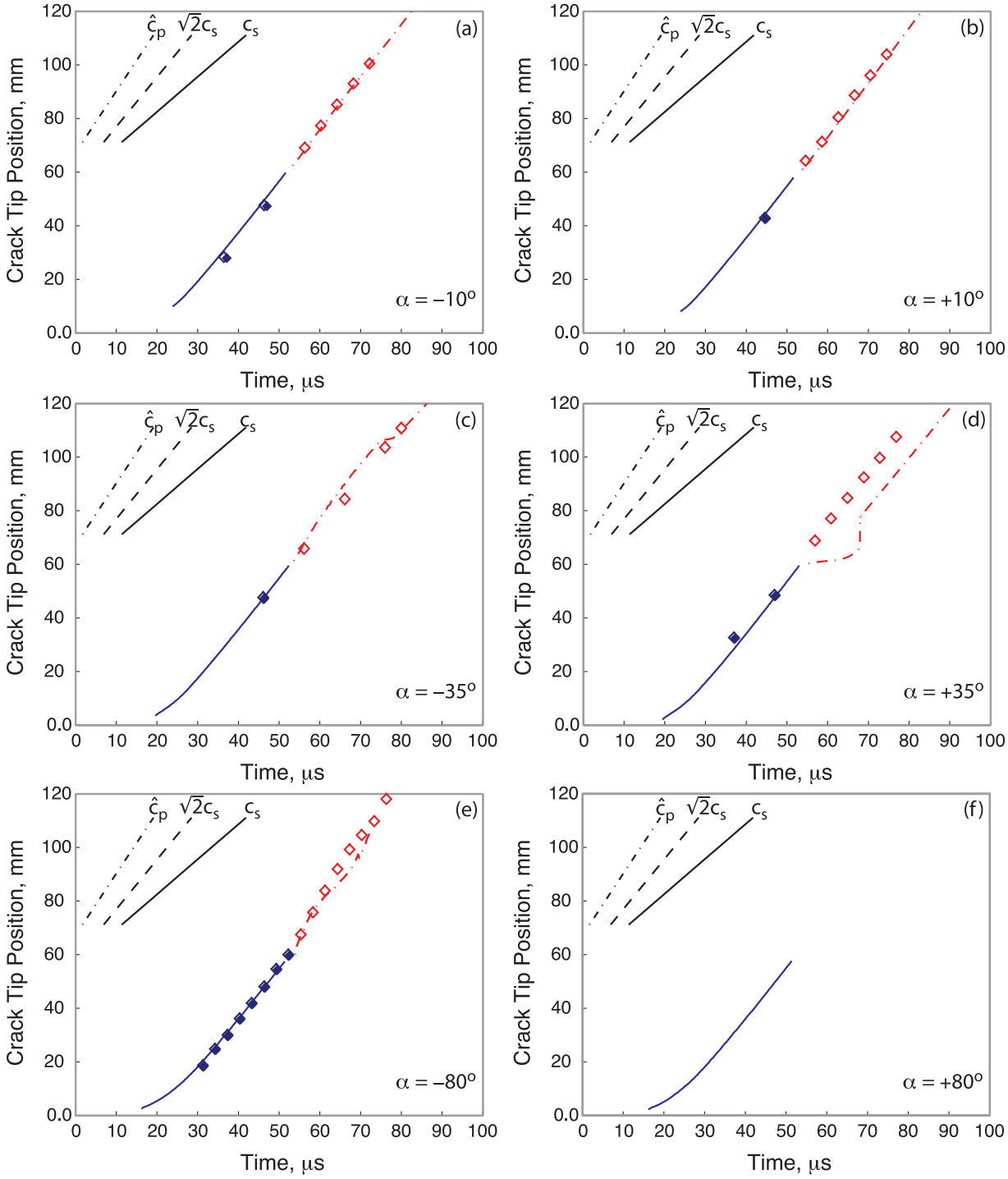

Figure 13. Comparison between finite element simulation results (solid lines for main fault and dotted lines for inclined fault) and experimental results (closed diamonds for main fault and open diamonds for inclined fault, when results are available) of crack tip position for kinked faults with branch angles of (a and b) ±10°, (c and d) ±35°, and (e and f) ±80°.

[25] The numerical analyses additionally provide the amount of slip accumulation during rupture along the fault segments. Figure 14 shows the accumulated slip during rupture for the six kink angles studied. The 10° kink cases show a large amount of slip accumulation along the inclined faults, with slip along the kink approaching the amount of slip that occurs on the main fault. The 35° cases have decreased slip along the inclined fault compared with the amount of slip that would occur along a horizontal extension of the main fault. For the 80° kink to the extensional side, rupture propagation struggled along the main fault, and slip only reached D_c, the critical slip-weakening distance, along a small portion of the rupture length, and complete

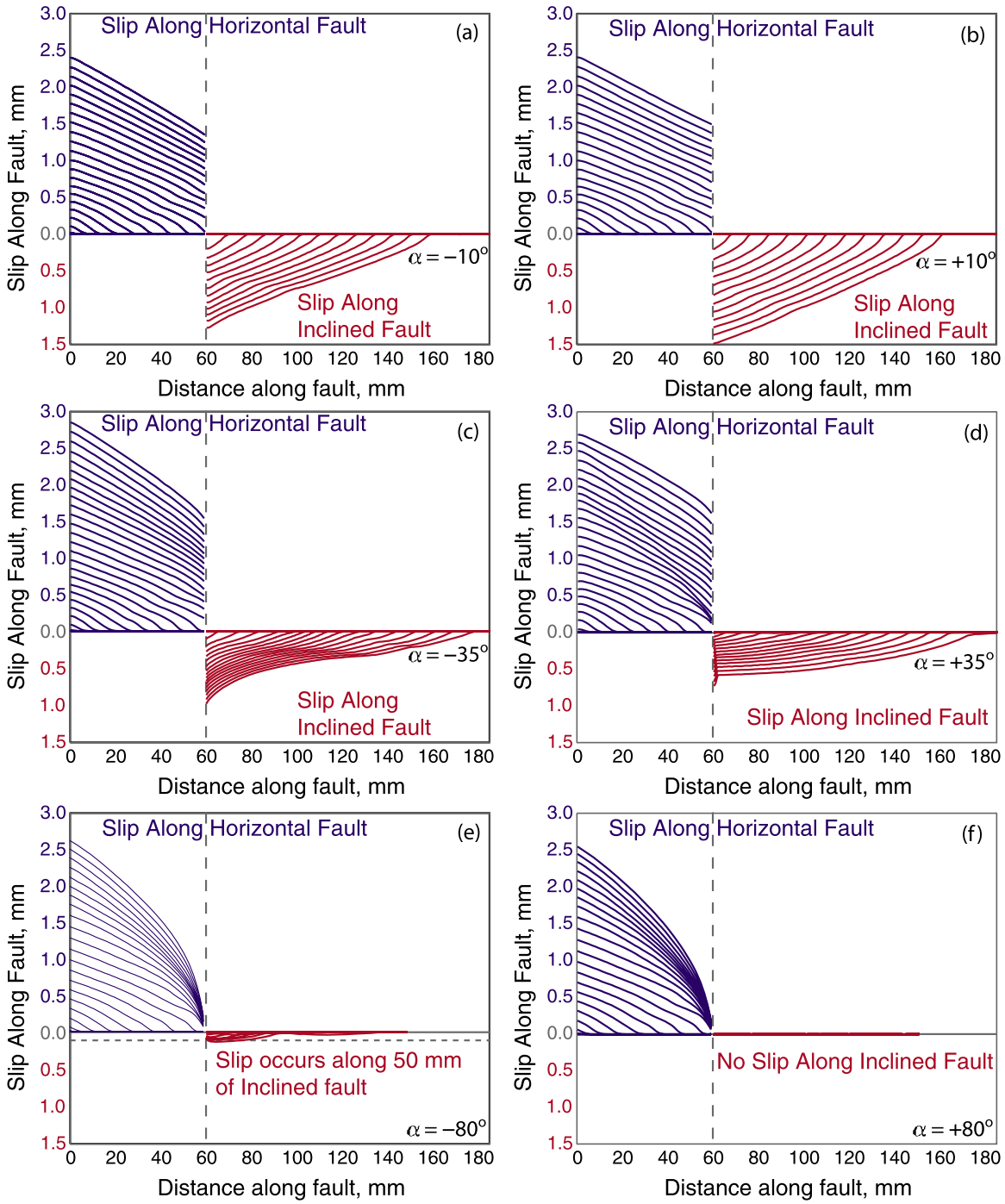

Figure 14. Amount of slip accumulation during rupture along faults with a kink with kink angles of (a and b) ±10°, (c and d) ±35°, and (e and f) ±80°.

weakening of the fault does not occur along the entire length of the rupture.

4.2. Branching Faults

[26] In the experiments involving rupture along a fault with a branching junction, three distinct dynamic path selection behaviors are observed: no branch activation, exclusive branching with no continuation of rupture on the main fault, and branch activation with rupture continuation along the main fault. The numerical simulations only display two of those behaviors; no branching and branching with rupture continuation along the main fault. Exclusive branching does not occur within these numerical analyses. Otherwise the numerical simulations show consistent results with the experiments, with some exceptions to be discussed.

[27] Isochromatic fringe patterns for both the experimental and numerical results, as shown in Figures 15 and 16, indicate that no branching occurs for a compressional branch angle of 10°. A Mach front can be clearly seen along the horizontal fault after the branching junction, but there is no Mach front along the inclined fault. The isochromatic fringe patterns indicate that the rupture prop-

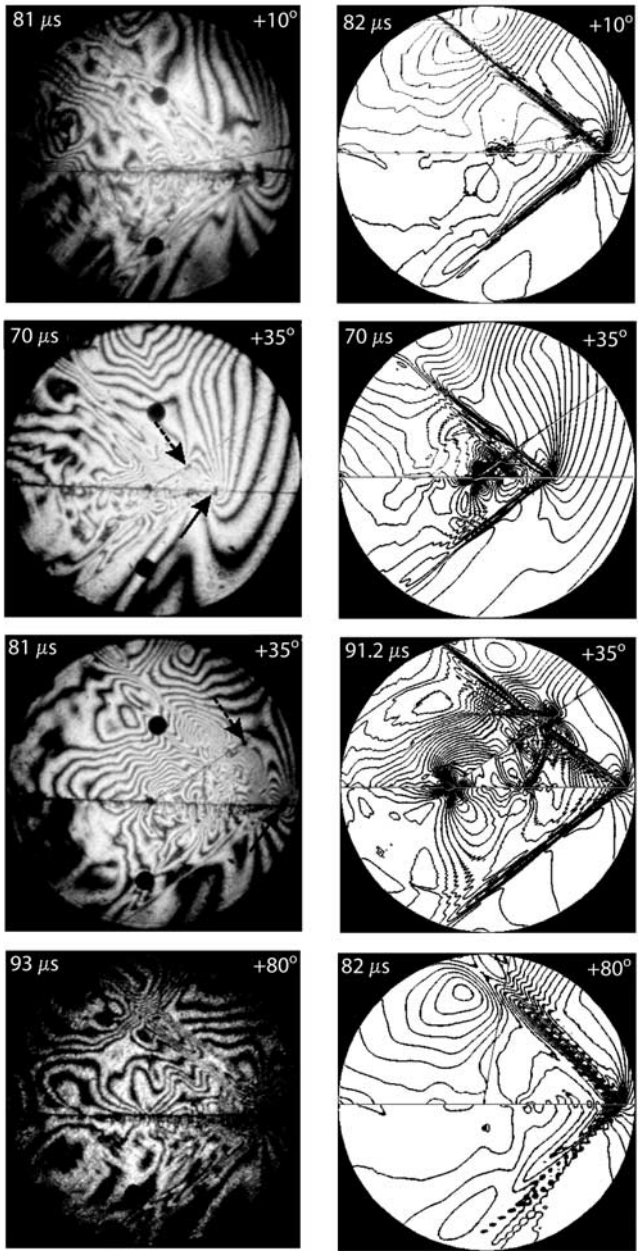

Figure 15. Comparison between (left) photographs of isochromatic fringe patterns and (right) finite element simulation results for branched faults with the inclined branch on the compressional side.

agates along the horizontal fault only and that no branching occurs. For the 10° extensional branch, the stress contours produced by the simulation display a Mach front along the inclined fault as well as the horizontal continuation of the main fault. Although a postmortem examination of the specimens used in the experiment shows that the interface was still firmly bonded and unaffected by the incoming rupture, some slip does occur during the numerical simulations, but that slip is an order of magnitude less than the slip that occurs on the main fault. Shear stress on the inclined fault is brought to peak level by the intersection of the Mach front from the main fault with the branch and slip is initiated at this intersection. Figure 17 shows the slip along the inclined fault and the slip along the main fault. The slip along the inclined fault is less than the critical slip-weakening distance, D_c, indicating that the inclined fault never completely weakened. Figure 18 presents the evolution of crack tip position during experiments and during the numerical simulations for branches to both the compressional and extensional sides of the fault. For the branches inclined at ±10°, the crack tip position during rupture along both segments of the main fault match the experimental results well and shows that the rupture velocity and slip accumulation along the main fault are not altered by the presence of the branch.

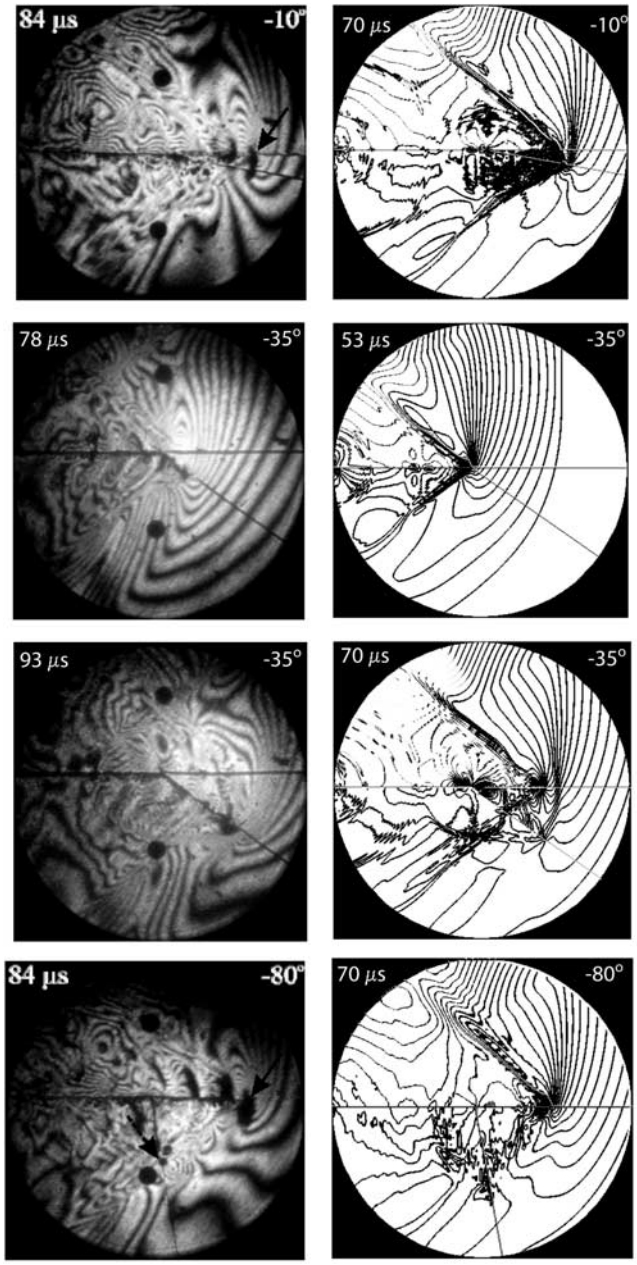

Figure 16. Comparison between (left) photographs of isochromatic fringe patterns and (right) finite element simulation results for branched faults with the inclined branch on the extensional side.

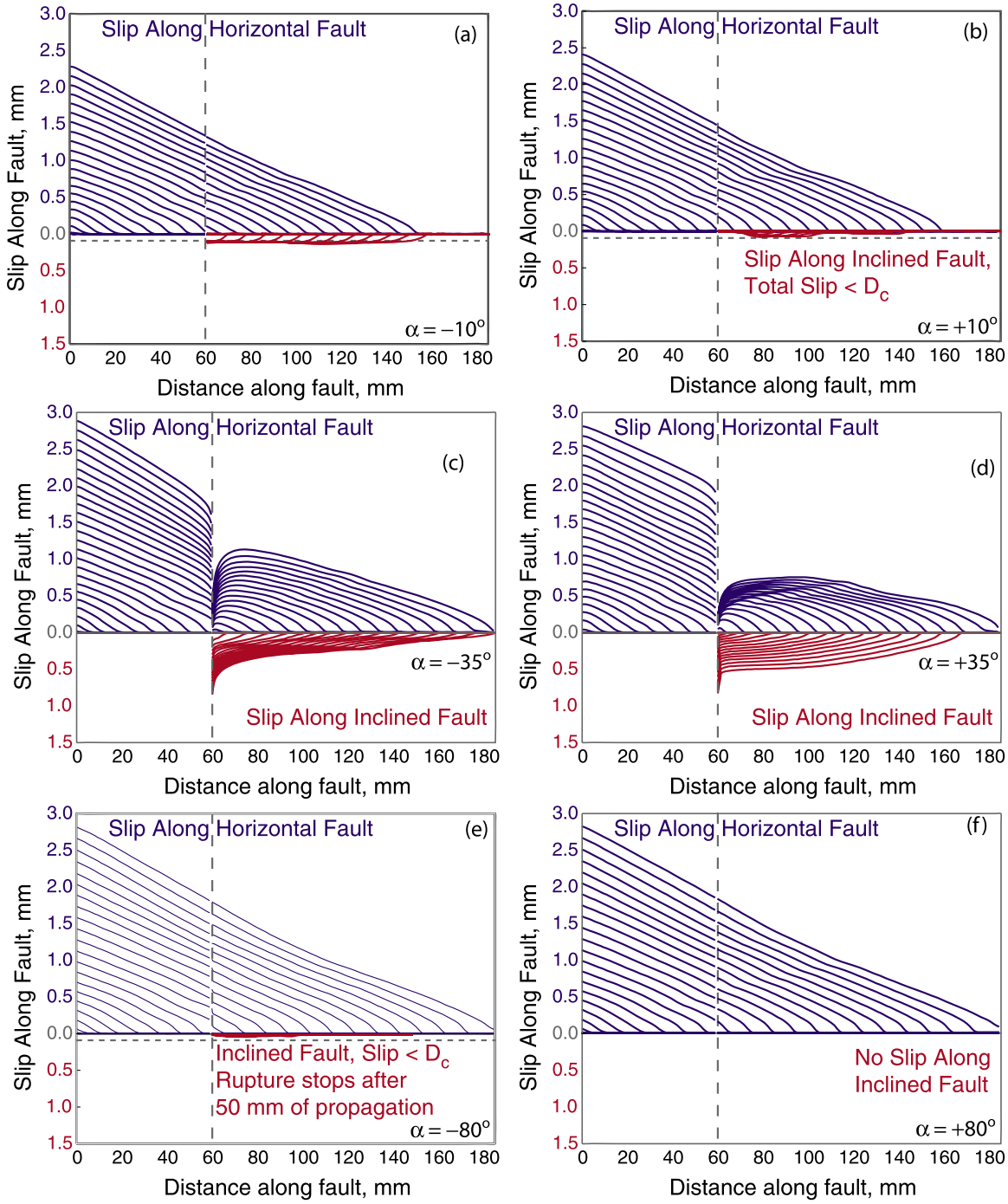

Figure 17. Amount of slip accumulation during rupture along faults with a branch with branch angles of (a and b) ±10°, (c and d) ±35°, and (e and f) ±80°.

[28] Continuation of the main fault causes substantial alteration in rupture along the branch compared with the bend case for a branch inclined at 35° to the compressional side. When the crack reaches the branch, it is propagating steadily at a supershear speed of approximately $1.6c_s$. After the crack reaches the branching junction, it begins to propagate along the inclined fault and continues to propagate along the horizontal main fault path. The rupture propagation velocity along the horizontal fault remains constant at approximately $1.6c_s$ past the branching junction. Rupture velocity on the inclined fault begins at a sub-Rayleigh speed. Initially, a distinct Mach front cannot be seen along the branch, and the rupture tip appears to travel in the Mach front of the rupture along the horizontal path. After the rupture has traveled approximately 30 mm along the inclined fault, it develops its own Mach front, and the rupture moves ahead of the Mach front from the horizontal fault, traveling close or slightly faster than the p wave speed. For this case there is excellent agreement between the experimental photographs and the numerical contours of the isochromatic fringe patterns, as is evident in Figure 15.

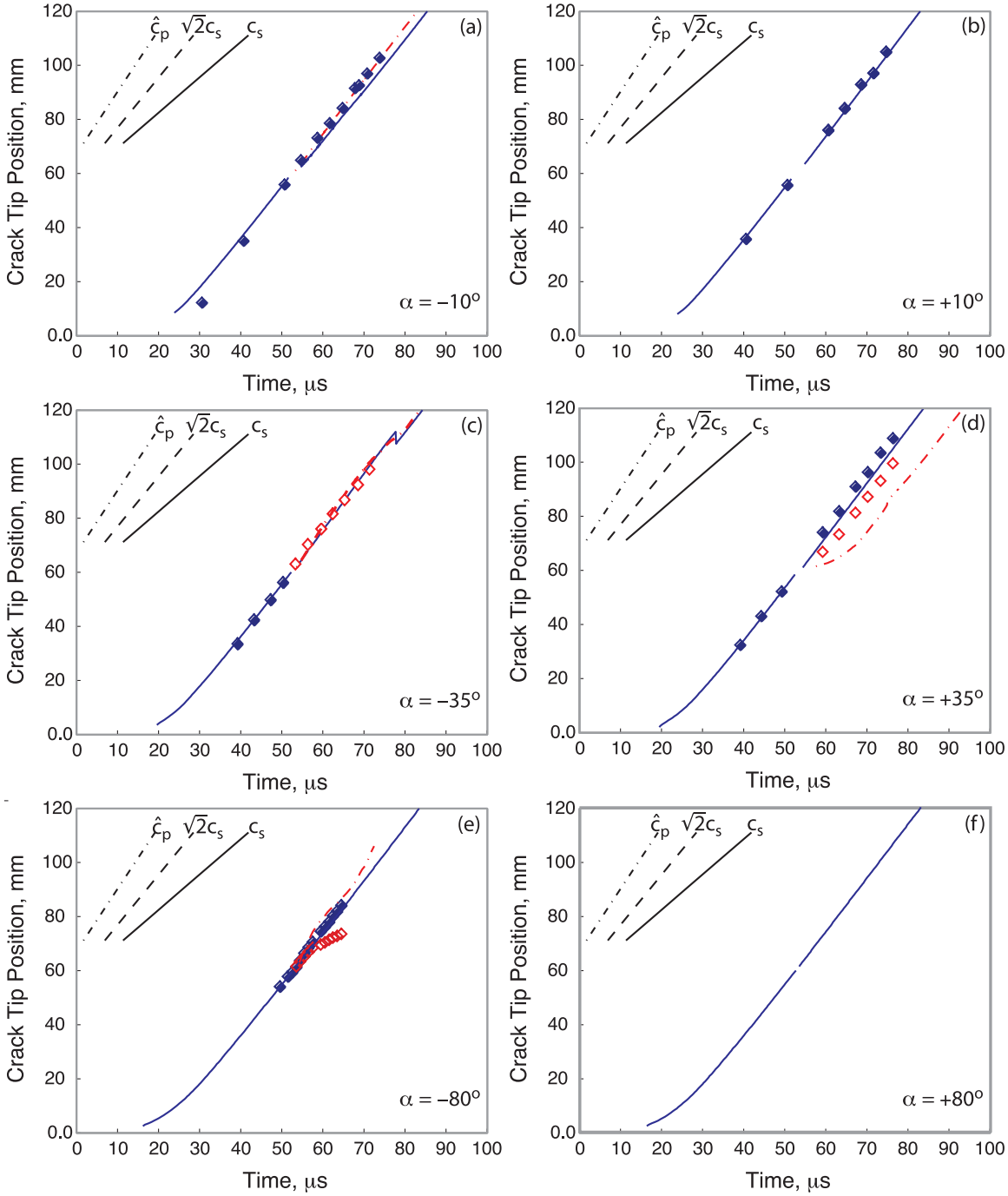

Figure 18. Comparison between finite element simulation results (solid lines for main fault and dotted lines for inclined fault) and experimental results (closed diamonds for main fault and open diamonds for inclined fault, when results are available) of crack tip position for branched faults with branch angles of (a and b) ±10°, (c and d) ±35°, and (e and f) ±80°.

[29] The numerical and experimental results differ for the branch at 35° to the extensional side. In the simulations, rupture propagation occurs along the inclined fault and continues to propagate along the horizontal main fault past the branching junction, and Mach fronts can be seen on each in the isochromatic fringe patterns in Figure 16. In the experiments, however, exclusive branching is seen and rupture stops along the horizontal fault after the branching junction. In the numerical simulations, the rupture propagation velocity along the inclined branch increases after the branching junction, and a substantial amount of slip accumulation occurs on the inclined fault.

[30] As in the kinked fault cases, a branch inclined at 80° to the compressional side is unfavorable for rupture propagation. In both the simulations and experiments, the crack bypasses the inclined fault, continuing along the main fault with steady supershear rupture velocity. In the finite element analysis, the extensional 80° branch is only activated for a

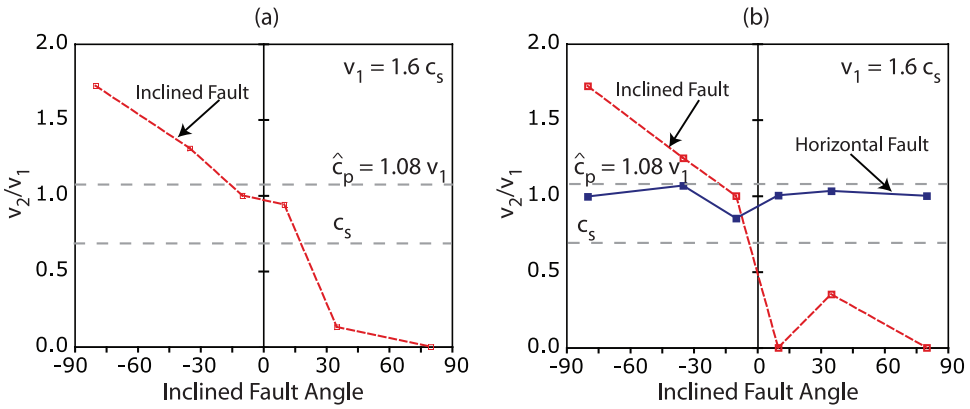

Figure 19. (a) Velocity along the inclined fault after the bend junction relative to the incoming velocity, $v_1 = 1.6c_s$. (b) Velocity along the inclined and horizontal segments of the fault after the branching junction relative to the incoming velocity, $v_1 = 1.6c_s$.

short distance and rupture continues along the main fault. Very little slip accumulates along the inclined fault, as in the kinked fault case, and rupture stops along the inclined fault in both the experiments and numerical simulations. The rupture along the branch stops propagating along the path when the crack has traveled 50 mm along the incline. The experiments show signs of tensile microcracks forming along the inclined fault [*Rousseau and Rosakis*, 2003, 2009]; however, this behavior cannot be captured within the finite element analyses conducted here. An examination of shear stress and accumulated slip produced during the numerical simulations along the inclined fault shows that slip is less than D_c, and complete weakening does not occur.

5. Discussion

[31] The experimental investigations of *Rousseau and Rosakis* [2003, 2009] showed that fault bends and branches, respectively, can cause large variations in rupture propagation velocity, and fault bends can serve as rupture termination points for some fault geometries. We find that numerical simulations of impact experiments using a frictional and cohesive slip-weakening law can reproduce the main results of both experimental studies.

[32] The presence of a kink or a branch in a fault path can cause an abrupt change in the rupture propagation velocity. For kinked faults, this has been observed numerically by *Aochi et al.* [2000a] and experimentally by *Rousseau and Rosakis* [2003]. Simulations by *Aochi et al.* [2000a] found that rupture velocity decreases after a compressional fault bend, and the decrease in rupture velocity depends on whether the bend is smooth or a sharp kink. Figure 19a shows the velocity immediately after the bend for all inclined fault angles considered here relative to the incoming rupture velocity. For fault geometries with a bend on the extensional side, rupture along the inclined fault is able to accelerate initially to levels above that of the incoming crack velocity due to fault opening stresses, $\sigma_{\theta\theta}$ becoming tensile and hence allowing opening. On the compressional side of the main fault, there is a decrease in rupture velocity relative to incoming rupture velocity as the inclined fault angle increases. This behavior agrees qualitatively with the experimental observations although there are some differences in the post bend junction velocity along the inclined fault due to neglect of the tensile strength of the bend in the finite element analyses.

[33] As in the numerical investigations of *Bhat et al.* [2007a] and the experimental studies of *Biegel et al.* [2007] on the effects of short branches on rupture propagation, we find that rupture activation along the branch causes alterations in the rupture velocity on the main fault. Observations of rupture velocity during the 2001 Kunlun earthquake by *Robinson et al.* [2006] and *Vallée et al.* [2008] demonstrated that a small change in strike along the fault corresponds to a change in rupture velocity, with rupture accelerating after encountering a small angle kink to the extensional side, and rupture decelerating after encountering a small kink angle to the compressional side. Figure 19b shows the velocity immediately after the branch junctions for all inclined fault angles considered relative to the incoming rupture velocity. Rupture velocity on the inclined fault for the branching cases follows the same trend as in the kinked fault cases. Those observations are consistent with the findings of *Vallée et al.* [2008] for the Kunlun earthquake. For the branched fault geometries, the rupture velocity on the horizontal continuation of the main fault immediately after the branching junction is approximately the same as the incoming rupture velocity for most branch angles. The numerical simulations also highlight the differences between a fault branch and a fault bend. In particular, for fault bend inclinations of 80° to the compressional or extensional sides, that bend can serve as a rupture termination point. On the extensional bend, rupture terminates after a short propagation distance of less than 50 mm, while the fault bend junction is the rupture endpoint for the compressional bend. However, when there is a branch instead at 80° to the compressional side, rupture continues along the main fault with no alteration in rupture velocity and no propagation along the branch.

[34] This study also allows us to compare the amount of slip accumulations along the inclined and main faults for both the kinking fault and branching fault scenarios. We find that for small kink angles, slip accumulation along the inclined fault segments is roughly the same as that accumulated along the main fault segments. As kink angle increases, that slip accumulated along the inclined fault

decreases relative to that along the main fault. However, this trend does not hold for branching fault geometries. For both small and large branch angles, rupture bypasses the inclined fault, or else accumulates very little slip along it, but for intermediate branch angles, the amount of slip accumulated along the inclined fault and the extension of the main fault is roughly even.

[35] Previous numerical and experimental studies as well as this study have focused on the role of complexities in preexisting fault geometries during a single rupture event and elastic off-fault deformation at bends and junctions. Seismic and geologic observations of effects of fault geometry on rupture propagation and extent along natural faults depend not only on the fault geometry and far field stresses, but also on the history of events. Numerical simulations by *Ando and Yamashita* [2007] have investigated the development of branched faults during shear rupture. *Duan and Oglesby* [2005, 2007] extended those works to include the long term effects of bends and branches on rupture dynamics, and found that stresses near the bend develop large differences from the regional stress field and those local stresses play a large role in controlling rupture dynamics. *Duan and Day* [2008] included inelastic deformation during dynamic rupture through fault kinks, and found that coseismic inelastic deformation surrounding fault kinks has large effects on residual stresses at those locations.

[36] This study and the experiments by *Rousseau and Rosakis* [2003, 2009] modeled here address the role of a complexity in the preexisting fault geometry during a single dynamic rupture within an elastic material. Future laboratory experiments could investigate the development of complexities in fault geometry as well as the role of stress evolution due to cycles of events.

6. Conclusions

[37] We conducted finite element analyses to numerically investigate the experiments of dynamic rupture in Homalite plates of *Rousseau and Rosakis* [2003, 2009] involving shear rupture along bonded interfaces with a fault bend and fault branch. We found that dynamic explicit 2-D plane-stress finite element analyses with a simple linear slip-weakening description of cohesive and frictional strength of the bonded interfaces can reproduce the qualitative rupture behavior past the bend and branch junctions in most cases. There is also good agreement between the numerical and experimental crack tip positions during rupture. The finite element results provide additional insight into differences in the amount of slip accumulation occurring on the main horizontal fault versus that occurring on the inclined fault bends or branched faults, and they indicate that slip along inclined faults can be substantially less, even with healthy rupture propagation, than slip along the main fault. Although results agree for the most part, differences between the numerical and experimental results exist for cases with a bend or branch along the extensional side perhaps due, at least in part, to mixed mode rupture microcrack formation in the bulk during the experiments which cannot be modeled within the simple cohesive and frictional laws implemented in this numerical study. Future studies could incorporate a tensile component of fault strength in the slip-weakening description to better match the experimental results.

[38] **Acknowledgments.** All authors except A.J.R. and C.-E.R. were supported at Harvard by NSF-EAR grants 0440145 and/or 0809610 and by the Southern California Earthquake Center, which is funded by cooperative agreements NSF-EAR 0106924 and USGS 02HQAG0008 (this is SCEC contribution 1229). A.J.R. and C.-E.R. were supported by U.S. DOE grant DE-FG52-06NA26209, NSF-EAR grant EAR-0711545, and ONR MURI grant N0014-06-1-0730.

References

Aagaard, B. T., and T. H. Heaton (2004), Near-source ground motions from simulations of sustained intersonic and supersonic fault ruptures, *Bull. Seismol. Soc. Am.*, *94*(6), 2064–2078.

ABAQUS, Inc. (2005), ABAQUS documentation, version 6.5, Providence, R. I.

Adda-Bedia, M., and R. Madariaga (2008), Seismic Radiation from a Kink on an Antiplane Fault, *Bull. Seismol. Soc. Am.*, *98*(5), 2291–2302, doi:10.1785/0120080003.

Ando, R., and T. Yamashita (2007), Effects of mesoscopic-scale fault structure on dynamic earthquake ruptures: Dynamic formation of geometrical complexity of earthquake faults, *J. Geophys. Res.*, *112*(B9), B09303, doi:10.1029/2006JB004612.

Ando, R., N. Kame, and T. Yamashita (2007), An efficient boundary integral equation method applicable to the analysis of non-planar fault dynamics, *Earth Planets Space*, *59*(5), 363–373.

Andrews, D. J. (1976), Rupture velocity of plane strain shear cracks, *J. Geophys. Res.*, *81*(32), 5679–5687.

Aochi, H., E. Fukuyama, and M. Matsu'ura (2000a), Spontaneous rupture propagation on a non-planar fault in 3-D elastic medium, *Pure Appl. Geophys.*, *157*(11–12), 2003–2027.

Aochi, H., E. Fukuyama, and M. Matsu'ura (2000b), Selectivity of spontaneous rupture propagation on a branched fault, *Geophys. Res. Lett.*, *27*(22), 635–638.

Archuleta, R. J. (1984), A faulting model for the 1979 Imperial Valley earthquake, *J. Geophys. Res.*, *89*(B6), 4559–4585.

Bhat, H. S., R. Dmowska, J. R. Rice, and N. Kame (2004), Dynamic slip transfer from the Denali to Totschunda faults, Alaska: Testing theory for fault branching, *Bull. Seismol. Soc. Am.*, *94*(6), S202–S213, doi:10.1785/0120040601.

Bhat, H. S., R. Dmowska, G. C. P. King, Y. Klinger, and J. R. Rice (2007a), Off-fault damage patterns due to supershear ruptures with application to the 2001 M_w 8.1 Kokoxili (Kunlun) Tibet earthquake, *J. Geophys. Res.*, *112*, B06301, doi:10.1029/2006JB004425.

Bhat, H. S., M. Olives, R. Dmowska, and J. R. Rice (2007b), Role of fault branches in earthquake rupture dynamics, *J. Geophys. Res.*, *112*, B11309, doi:10.1029/2007JB005027.

Biegel, R. L., C. G. Sammis, and A. J. Rosakis (2007), Interaction of a dynamic rupture on a fault plane with short frictionless fault branches, *Pure Appl. Geophys.*, *164*(10), 1881–1904, doi:10.1007/s00024-007-0251-2.

Bouchon, M., and H. Karabulut (2008), The aftershock signature of supershear earthquakes, *Science*, *320*(5881), 1323–1325, doi:10.1126/science.1155030.

Bouchon, M., and M. Vallée (2003), Observation of long supershear rupture during the magnitude 8.1 Kunlunshan earthquake, *Science*, *301*(5634), 824–826, doi:10.1126/science.1086832.

Bouchon, M., N. Toksöz, H. Karabulut, M. Bouin, M. Dietrich, M. Aktar, M. Edie, and A. Mustafa (2000), Seismic imaging of the 1999 Izmit (Turkey) rupture inferred from the near-fault recordings, *Geophys. Res. Lett.*, *27*(18), 3013–3016.

Bouchon, M., M. P. Bouin, H. Karabulut, M. N. Toksoz, M. Dietrich, and A. J. Rosakis (2001), How fast is rupture during an earthquake? New insights from the 1999 Turkey earthquakes, *Geophys. Res. Lett.*, *28*(14), 2723–2726.

Burridge, R., G. Conn, and L. B. Freund (1979), The stability of a rapid mode II shear crack with finite cohesive traction, *J. Geophys. Res.*, *84*(B5), 2210–2222.

Duan, B., and S. M. Day (2008), Inelastic strain distribution and seismic radiation from rupture of a fault kink, *J. Geophys. Res.*, *113*, B12311, doi:10.1029/2008JB005847.

Duan, B., and D. D. Oglesby (2005), Multicycle dynamics of nonplanar strike-slip faults, *J. Geophys. Res.*, *110*, B03304, doi:10.1029/2004JB003298.

Duan, B., and D. D. Oglesby (2007), Nonuniform prestress from prior earthquakes and the effect on dynamics of branched fault systems, *J. Geophys. Res.*, *112*, B05308, doi:10.1029/2006JB004443.

Dunham, E. M., and R. J. Archuleta (2004), Evidence for a supershear transient during the 2002 Denali fault earthquake, Bull, *Seismol. Soc. Am.*, *94*(6B), S256–S268, doi:10.1785/0120040616.

Ellsworth, W. L., M. Celebi, J. R. Evans, E. G. Jensen, R. Kayen, M. C. Metz, D. J. Nyman, J. W. Roddick, P. Spudich, and C. D. Stephens (2004), Near-field ground motion of the 2002 Denali fault, Alaska, earthquake recorded at pump station 10, *Earthq. Spectra*, *20*(3), 597–615.

Fliss, S., H. S. Bhat, R. Dmowska, and J. R. Rice (2005), Fault branching and rupture directivity, *J. Geophys. Res.*, *110*, B06312, doi:10.1029/2004JB003368.

Freund, L. B. (1990), *Dynamic Fracture Mechanics*, Cambridge Univ. Press, New York.

Harris, R. A., and S. M. Day (1993), Dynamics of fault interaction: Parallel strike-slip faults, *J. Geophys. Res.*, *98*(B3), 4461–4472.

Harris, R. A., and S. M. Day (1999), Dynamic 3D simulations of earthquakes on en echelon faults, *Geophys. Res. Lett.*, *26*(14), 2089–2092.

Harris, R. A., R. J. Archuleta, and S. M. Day (1991), Fault steps and the dynamic rupture process: 2-D numerical simulations of a spontaneously propagating shear fracture, *Geophys. Res. Lett.*, *18*(5), 893–896.

Ida, Y. (1972), Cohesive force across the tip of a longitudinal-shear crack and Griffith's specific surface energy, *J. Geophys. Res.*, *77*(20), 3796–3805.

Kame, N., J. R. Rice, and R. Dmowska (2003), Effects of prestress state and rupture velocity on dynamic fault branching, *J. Geophys. Res.*, *108*(B5), 2265, doi:10.1029/2002JB002189.

King, G. C. P., and J. Nabelek (1985), Role of fault bends in the initiation and termination of earthquake rupture, *Science*, *228*(4702), 984–987.

Needleman, A., and A. J. Rosakis (1999), The effect of bond strength and loading rate on the conditions governing the attainment of intersonic crack growth along interfaces, *J. Mech. Phys. Solids*, *47*(12), 2411–2449.

Palmer, A. C., and J. R. Rice (1973), Growth of slip surfaces in progressive failure of over-consolidated clay, *Proc. R. Soc. London, Ser. A*, *332*(1591), 527–548.

Poliakov, A. N. B., R. Dmowska, and J. R. Rice (2002), Dynamic shear rupture interactions with fault bends and off-axis secondary faulting, *J. Geophys. Res.*, *107*(B11), 2295, doi:10.1029/2001JB000572.

Robinson, D. P., C. Brough, and S. Das (2006), The M_w 7.8, 2001 Kunlunshan earthquake: Extreme rupture speed variability and effect of fault geometry, *J. Geophys. Res.*, *111*, B08303, doi:10.1029/2005JB004137.

Rosakis, A. J. (2002), Intersonic shear cracks and fault ruptures, *Adv. Phys.*, *51*(4), 1189–1257, doi:10.1080/00018730210122328.

Rosakis, A. J., and K. Ravi-Chandar (1986), On crack-tip stress state: An experimental evaluation of three-dimensional effects, *Int. J. Solids Struct.*, *22*(2), 121–134.

Rosakis, A. J., O. Samudrala, and D. Coker (1999), Cracks faster than the shear wave speed, *Science*, *284*(5418), 1337–1340, doi:10.1126/science.284.5418.1337.

Rosakis, A. J., G. Lykotrafitis, H. Kanamori, and K. Xia (2007), Speeds, directionality and modes, in *Treatise on Geophysics*, vol. 4, edited by G. Schubert, pp. 151–192, Elsevier, Amsterdam.

Rousseau, C.-E., and A. J. Rosakis (2003), On the influence of fault bends on the growth of sub-Rayleigh and intersonic dynamic shear ruptures, *J. Geophys. Res.*, *108*(B9), 2411, doi:10.1029/2002JB002310.

Rousseau, C.-E., and A. J. Rosakis (2009), Dynamic path selection along branched faults: Experiments involving sub-Rayleigh and supershear ruptures, *J. Geophys. Res.*, *114*, B08303, doi:10.1029/2008JB006173.

Samudrala, O., Y. Huang, and A. J. Rosakis (2002), Subsonic and intersonic shear rupture of weak planes with a velocity weakening cohesive zone, *J. Geophys. Res.*, *107*(B8), 2170, doi:10.1029/2001JB000460.

Segall, P., and D. D. Pollard (1980), Mechanics of discontinuous faults, *J. Geophys. Res.*, *85*(B8), 4337–4350.

Sibson, R. H. (1986), Rupture interactions with fault jogs, in *Earthquake Source Mechanics*, *Geophys. Monogr. Ser.*, vol. 37, edited by S. Das et al., pp. 157–167, AGU, Washington, D. C.

Spudich, P., and E. Cranswick (1984), Direct observation of rupture propagation during the 1979 Imperial Valley earthquake using a short baseline accelerometer array, *Bull. Seismol. Soc. Am.*, *74*(6), 2083–2114.

Templeton, E. L., and J. R. Rice (2008), Off-fault plasticity and earthquake rupture dynamics: 1. Dry materials or neglect of fluid pressure changes, *J. Geophys. Res.*, *113*, B09306, doi:10.1029/2007JB005529.

Vallée, M., M. Landés, N. M. Shapiro, and Y. Klinger (2008), The 14 November 2001 Kokoxili (Tibet) earthquake: High-frequency seismic radiation originating from the transitions between sub-Rayleigh and supershear rupture velocity regimes, *J. Geophys. Res.*, *113*, B07305, doi:10.1029/2007JB005520.

Wesnousky, S. G. (1988), Seismological and structural evolution of strike-slip faults, *Nature*, *335*(6188), 340–342.

Wesnousky, S. G. (2006), Predicting the endpoints of earthquake ruptures, *Nature*, *444*(7117), 358–360.

Xia, K., A. J. Rosakis, and H. Kanamori (2005), Supershear and subrayleigh to supershear transition observed in laboratory earthquake experiments, *Exp. Tech.*, *29*(3), 63–66.

Xia, K. W., A. J. Rosakis, and H. Kanamori (2004), Laboratory earthquakes: The sub-Rayleigh-to-supershear rupture transition, *Science*, *303*(5665), 1859–1861.

A. Baudet, 56 Avenue du Marechal Foch, F-78400 Chatou, France. (aurelie_baudet1@hotmail.com)

H. S. Bhat, Department of Earth Sciences, University of Southern California, Zumberge Hall of Science, 264B, 3651 Trousdale Parkway, Los Angeles, CA 90089, USA. (hbhat@usc.edu)

R. Dmowska and J. R. Rice, Department of Earth and Planetary Sciences, Harvard University, 227 Pierce Hall, 29 Oxford Street, Cambridge, MA 02138, USA. (dmowska@esag.harvard.edu; rice@esag.harvard.edu)

A. J. Rosakis, Graduate Aeronautical Laboratories, California Institute of Technology, 1200 East California Boulevard, Mail Code 105-50, Pasadena, CA 91125, USA. (rosakis@aero.caltech.edu)

C.-E. Rousseau, Department of Mechanical Engineering, University of Rhode Island, 222-B Wales Hall, Kingston, RI 02881, USA. (rousseau@uri.edu)

E. L. Templeton, School of Engineering and Applied Sciences, Harvard University, 327 Pierce Hall, 29 Oxford Street, Cambridge, MA 02138, USA. (templet@fas.harvard.edu)